

2009

Ultrafast-time-gated ballistic-photon imaging and shadowgraphy in optically dense rocket sprays

Zane Donald Schaefer
Iowa State University

Follow this and additional works at: <https://lib.dr.iastate.edu/etd>

 Part of the [Mechanical Engineering Commons](#)

Recommended Citation

Schaefer, Zane Donald, "Ultrafast-time-gated ballistic-photon imaging and shadowgraphy in optically dense rocket sprays" (2009).
Graduate Theses and Dissertations. 10626.
<https://lib.dr.iastate.edu/etd/10626>

This Thesis is brought to you for free and open access by the Iowa State University Capstones, Theses and Dissertations at Iowa State University Digital Repository. It has been accepted for inclusion in Graduate Theses and Dissertations by an authorized administrator of Iowa State University Digital Repository. For more information, please contact digirep@iastate.edu.

**Ultrafast-time-gated ballistic-photon imaging and shadowgraphy in optically
dense rocket sprays**

by

Zane Donald Schaefer

A thesis submitted to the graduate faculty
in partial fulfillment of the requirements for the degree of
MASTER OF SCIENCE

Major: Mechanical Engineering

Program of Study Committee:
Terrence R. Meyer, Major Professor
Song-Charng Kong
Hui Hu

Iowa State University

Ames, Iowa

2009

TABLE OF CONTENTS

LIST OF FIGURES	iii
LIST OF TABLES	iv
ABSTRACT	v
CHAPTER 1. INTRODUCTION AND BACKGROUND	1
1.1 Sprays	1
1.2 Imaging	5
CHAPTER 2. EXPERIMENTAL SET-UP	9
2.1 Optical Set-Up	9
2.2 Nozzle Set-Up	13
CHAPTER 3. IMAGE PROCESSING	18
CHAPTER 4. RESULTS	20
4.1 Injector A	20
4.2 Injector B	23
4.3 Injector C	33
4.4 Injector D	35
4.5 Injector E	36
4.6 Injector F	37
4.7 Injector Comparison	38
CHAPTER 5. SUMMARY AND DISCUSSION	42
BIBLIOGRAPHY	43
ACKNOWLEDGEMENTS	48

LIST OF FIGURES

Figure 1. Depiction of breakup modes.....	2
Figure 2. Schematic of co-axial swirl injector and conceptual view of the spray structure. ...	4
Figure 3. X-ray versus visible-light snapshots of two different types of spray. (22)	7
Figure 4. Typical imaging modes including planar sheet imaging (a) and line sight imaging (b).....	11
Figure 5. (a) Ballistic imaging concept showing photon path of ballistic, snake, and diffuse light (left) and conceptual time trace of photons exiting the spray (right). (b) Schematic of ballistic-imaging system.	12
Figure 6. Swirl-coaxial liquid rocket injector.	15
Figure 7. Injector nozzles with exit diameters of (a) 5.4 mm, (b) 7.6 mm, (c) 9.1 mm, (d) 8.1 mm, (e) 10.2 mm, and (f) 10 mm.....	15
Figure 8. Non-Normalized (left) and Normalized (right) Ballistic Images for Injector A. ...	19
Figure 9. Ballistic images (top row) and ultrafast shadowgraph images (bottom row) for Injector A.	21
Figure 10. Ballistic images (top row), ultrafast shadowgraph images (bottom row), and corresponding PDF's for Injector A. Symbol © designates location for statistical analyses, two nozzle diameters downstream of nozzle exit.....	24
Figure 11. (a) Normalized mean intensity and (b) standard deviation as function of water flow rate for both ballistic imaging and ultrafast shadowgraphy. Data collected two nozzle diameters downstream of nozzle exit.	29
Figure 12. Ballistic images (top row) and ultrafast shadowgraph images (bottom row) for Injector B.	31
Figure 13. Ballistic images for Injector B at 1.1 lpm water and 410 lpm air. Top and bottom rows represent cases in which the injector has been rotated as indicated above.	33
Figure 14. Ballistic images (top row) and ultrafast shadowgraph images (bottom row) for Injector C, showing a series of images at the same flow condition.....	34
Figure 15. Ballistic images (top row) and ultrafast shadowgraph images (bottom row) for Injector D.	36
Figure 16. Ballistic images (top row) and ultrafast shadowgraph images (bottom row) for Injector E.....	37
Figure 17. Ballistic images for Injector F.	38
Figure 18. Nozzle geometries used in previous ballistic imaging discussions. Nozzles are illustrated in (a) and relevant parameters are listed in (b).	39
Figure 19. Ballistic imaging study of different nozzle injectors, where A, B, and C refer to geometries listed in Figure 18.....	40
Figure 20. Breakup trends in air–liquid momentum flux ratio.	41

LIST OF TABLES

Table 1. Rocket injector design parameters.	16
Table 2. Flow conditions.	16

ABSTRACT

Understanding the process of liquid-core breakup in optically dense sprays is critical for the development of predictive models in a variety of combustion engine applications. One of the limitations of current optical techniques is the inability to extract information on internal spray dynamics within regions shrouded by a dense cloud of droplets. Similar difficulties are faced with the use of any technique based on path-integrated absorption, such as X-ray radiography. Recently, a technique referred to as ballistic imaging, has been shown to improve the visualization of liquid-core breakup in dense sprays by employing an ultrafast time gate to discriminate against diffuse light. The goal of this work is to improve on the existing imaging system and investigate the breakup mechanisms of the liquid core immediately following injection. By reducing the contribution from photons that exit the spray after undergoing multiple scattering events, it is possible to emphasize the contribution from photons that undergo little to no scattering (ballistic photons). In the current work, the ballistic imaging technique is used in optically dense rocket sprays with light attenuation levels of 97% to 99%. The images collected in this manner reveal a variety of breakup mechanisms, with coherent liquid-core structures dominating the near-nozzle region. Through comparisons with conventional (non-time-gated) shadowgraph images, it is shown that these coherent structures are surrounded by a dense cloud of droplets. Tests were conducted for a variety of nozzle geometries and a range of flow conditions. In addition to investigating trends in the liquid breakup process, it is also observed that the internal nozzle flow within the injector can have a significant effect on the subsequent spray structure under certain flow conditions.

CHAPTER 1. INTRODUCTION AND BACKGROUND

This chapter gives a brief introduction and background of topics useful in understanding the current research. Information will be reviewed relating to rocket sprays and their atomization. A discussion on imaging techniques and their utilization will also be included. Shadowgraphy and ballistic photon imaging methods will be specifically detailed to show how each can be applied to current work.

1.1 Sprays

Liquid sprays are essential to the fuel-air mixture preparation processes in a variety of combustors. Research continues to progress as there is demand for more efficient and less polluting combustion processes. The way in which fuel is distributed from the injector directly affects emissions. Nonuniform fuel-droplet distributions can possibly cause hot spots and increase heat transfer to the combustion chamber wall. This in turn could cause significant damage. Fuel mixing also has a very large effect on the combustion process. In areas where the fuel to air ratio is overly rich in fuel, large amounts of soot can be produced. If the mixture is pushed outside the flammability limits of the fuel, quenching occurs and the excessive production of hydrocarbon and CO emissions begins. Even if the fuel air mixture is not rich problems can arise. Areas where the fuel to air ratio is near stoichiometric can produce significant amounts of NO_x emissions if coupled with a high combustion temperature (1). All of these potential combustion problems can be traced back the breakup process of the injected fuel.

The physical breakup process is shown in Figure 1. which includes three breakup modes. In Figure 1(a) the Rayleigh breakup regime is shown. This regime occurs at

relatively low injection velocities and is governed by the inertia forces acting on the oscillating liquid and by its surface tension. The breakup length is many nozzle diameters downstream from the nozzle exit and the resulting droplets diameters are generally greater than the nozzle diameter.

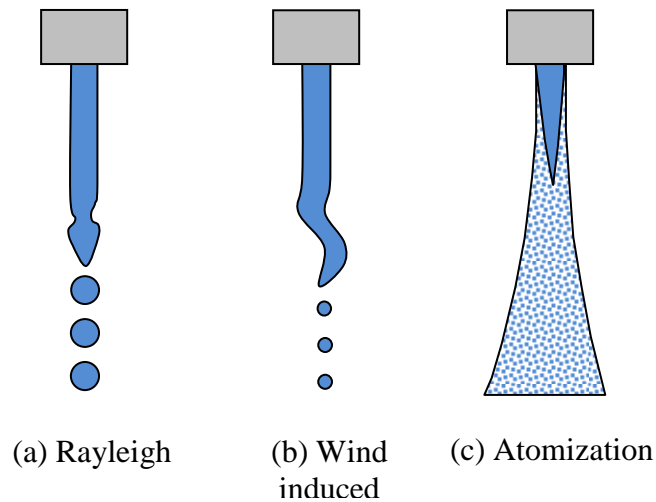


Figure 1. Depiction of breakup modes.

In the wind induced breakup, shown in Figure 1(b), the inertia of the gas phase becomes more important. Surface disturbances, caused by gas liquid interactions, form waves that increase in amplitude and eventually lead to breakup. The average droplet diameter decreases and is near that of the nozzle orifice diameter. While in the wind induced regime, as the relative velocity increases between the liquid and gas so do the aerodynamic forces acting on the liquid. These intensified forces increase wave amplitude and decrease wavelength. This leads a decrease in mean droplet diameter and the length it takes the stream to breakup.

With increased gas densities and large injection velocities the atomization regime is attained. In the atomization mode there are two distinct breakup lengths, which are shown in Figure 1(c). The first, surface breakup, begins directly at the nozzle exit. The second is an intact core that may continue several nozzle diameters downstream. During this regime the entire spray forms a conical shape and the average droplet diameter measures much smaller than the nozzle diameter. Despite differences in breakup modes all three regimes retain a similar region directly following the nozzle exit. In this region the spray is very dense making it extremely difficult to perform a detailed experimental assessment.

To simulate rocket combustor fuel injection in the current work, water and air are used in place of liquid oxygen and gaseous hydrogen. The water and air are introduced into the combustion chamber through a single gas-centered co-axial swirl injector and as they exit the nozzle, a number of breakup mechanisms, described above, occur. As shown in Figure 2 gas enters the center passage of the injector while liquid travels along the outer jacket and is injected from the side through the nozzle near the downstream section. The liquid passages are oriented in swirl pattern so that the liquid is injected tangentially along the inner diameter of the nozzle. The liquid forms a film along the interior passage walls as the gas flows over it at high relative velocities. Depending on the flow conditions, this film undergoes a variety of breakup regimes, and the final state of atomization has a significant impact on the heat release and combustion dynamics affecting the rocket injector.

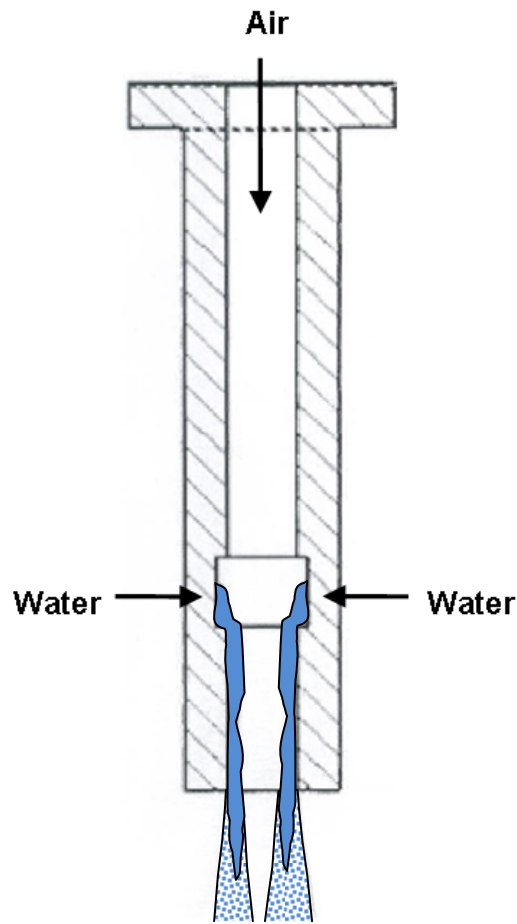


Figure 2. Schematic of co-axial swirl injector and conceptual view of the spray structure.

At flow rates where the relative velocity between the gas and liquid is small the primary breakup mode is Rayleigh breakup. As the liquid film progresses down the injector passage it begins to oscillate. Upon exit of the nozzle orifice the inertia forces overcome the surface tension of the liquid and it breaks into large fluid fragments. This breakup usually occurs many liquid-hole diameters downstream. When the flow rates are such that a moderate relative velocity is achieved, the wind induced regime is entered. During this regime the gas flowing over the liquid film causes surface disturbances that progress down

the fluid stream. As the fluid exits the nozzle these disturbances continue to increase in amplitude and eventually lead to breakup. In this breakup, referred to primary breakup, a dense liquid column begins to stretch into elongated ligaments. Elongated ligaments then break into fluid fragments whose mean diameters are generally close to that of the nozzle orifice. High relative velocities between the gas and liquid lead to the atomization regime. In the atomization regime fluid fragments are formed as the gas rushes over the thin liquid film. These fragments breakup into clouds of droplets in secondary breakup (2-5). After exit from the nozzle orifice the droplet clouds then become vapor, mix with the oxidizer, and combust. While surface breakup is apparent at the orifice exit a liquid core remains intact for several nozzle diameters downstream. The presence of an intact core at the nozzle exit during all breakup modes makes experimental assessment very difficult.

1.2 Imaging

A number of advanced techniques have been utilized for analyzing dilute sprays, including double-pulse holography, laser-induced fluorescence, schlieren photography, and shadowgraphy (6-13). Conventional shadowgraphy can provide some insight into the breakup mechanisms located near the edge or in voids of an optically dense spray. By passing a collimated light source through the spray and taking a quick image, certain aspects of spray-atomization can be deduced. Fluid ligaments and fragments that are shearing off the edge of a spray can be identified. Clouds of droplets can be identified as diffuse regions of attenuated light (14-17). Even though shadowgraphy does not provide very much detail about the optically dense core of a spray, it does provide a useful tool to support other imaging techniques.

As noted earlier, the goal of this work is to improve image contrast in the optically dense region of sprays, and hence a review of a wide variety of measurement techniques for dilute sprays, such as laser-induced fluorescence, holography, and schlieren imaging, is not included here in great detail beyond the aforementioned overview. Recent progress on imaging of dense sprays has been made on several fronts. The research group at Argonne National Laboratory has utilized radiography to capture time-resolved two-dimensional images of X-ray absorption using a synchrotron facility (18-22). This approach has many advantages, although it is currently limited to low temperature conditions and requires a synchrotron facility.

The system used to generate two-dimensional images from X-rays usually starts with a X-ray beam that is generated from an electron storage ring. To produce images the beam is controlled by a shutter and then exposed to the liquid spray. A scintillator crystal converts the transmitted X-rays into visible light which is imaged onto charge-coupled device (CCD) camera. The image contrast that is captured by the CCD comes from boundaries and interfaces between materials with different refraction indexes. Abrupt thickness variations in the absorption of X-rays can also indicate a gas-liquid boundary (22).

Images provided by Wang et al. (22), shown in Figure 3 below, compare traditional shadowgraphy to X-ray images for identical conditions and injectors. Frames c, e, g, and i show shadowgraphy images while frames d, f, h, and j show the corresponding X-ray images, respectively. It is easy to see that the X-ray images give great insight about the flow characteristics in the optically dense core section of the spray. In the X-ray images however, it is difficult to discern between areas a turbulent solid core and broken fluid fragments. This is apparent when comparing frames i and j. It appears in frame j that the flow is turbulent

and uniform throughout the entire picture. After viewing frame i it becomes apparent that the flow is not uniform but begins to break into fragments and voids as it moves downstream. The inability to distinguish between these regions in X-ray images is why it is best coupled with another imaging system.

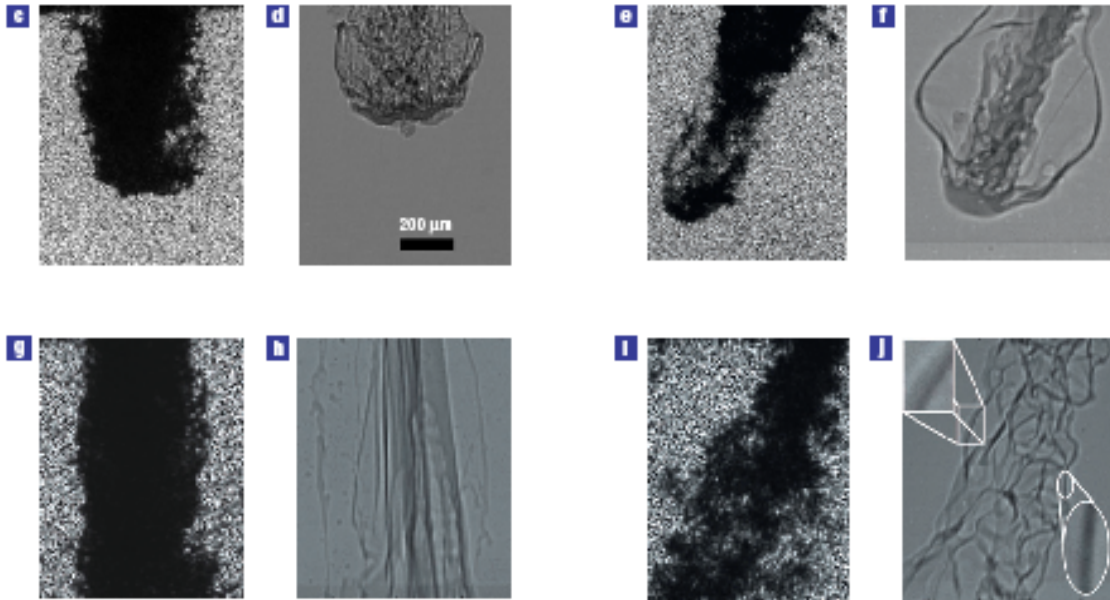


Figure 3. X-ray versus visible-light snapshots of two different types of spray. (22)

In the current work, it is shown that a tabletop ultrafast laser source with ultrafast time gating can be employed for near-field imaging of dense sprays. Because of its ability to preferentially image the droplet field or liquid-core structures, the types of images generated with this approach differ markedly from X-ray radiography, which is path averaged and does not employ photon discrimination. Ultrafast time gating can enhance the visualization of liquid-core evolution and break-up in optically dense sprays. Hence, it complements the X-

ray visualization techniques being developed using synchrotron facilities and is ultimately not limited to low-temperature conditions.

Referred to as time-gated ballistic imaging, this approach utilizes the temporal signature of light that propagates through various phases of a dense spray to distinguish droplets from liquid-core structures (23-27). In a region of the spray dominated by droplets, photons will undergo multiple scattering and travel more slowly through the spray. Photons that undergo minimal to no scattering (ballistic photons) or multiple forward scattering (snake photons) will travel more quickly through this same region. By preferentially gating the image using a two-picosecond optical Kerr-effect (OKE) shutter (28-30), it is possible to select the ballistic and snake photons to reduce the influence of diffuse light scattering from the droplets. The end result is a shadowgraph with significant contrast enhancement between various phases of the liquid breakup process. Because the signal from droplets is reduced with ballistic imaging, this technique cannot be used to track the local fluid mass fraction. However, when combined with conventional shadowgraphy, the images produced using this approach reveal information on the qualitative structure of the spray.

To assess the effectiveness of ballistic imaging, data with and without time gating are compared using a gas-centered swirl-coaxial injector with asymmetric nozzle-exit properties. The data reveal certain spray patterns that are dependent upon the interior flow of the injector prior to the nozzle exit plane. Hence, it is demonstrated that the use of an ultrafast laser source and a picosecond time gate can reveal important features of dense sprays that may otherwise not be discernable using other techniques.

CHAPTER 2. EXPERIMENTAL SET-UP

The optical and nozzle experimental set-up utilized during this research will be discussed in the following sections. The optical configuration is a ballistic-imaging system that is modified from previous studies. Comparisons are made to non-time-gated shadowgraphy to assess the effectiveness of time gating. The optical setup for non-time-gated shadowgraphy is nearly identical to that of ballistic imaging except that the time gate is removed. Six different nozzles with varying geometries were supplied by the Air Force Research Laboratory and were tested under various flow conditions.

2.1 Optical Set-Up

Ballistic imaging uses line of sight imaging where the beam is imaged directly into the camera as detailed in Figure 4. Another common imaging configuration uses planar sheet illumination where the camera is positioned perpendicular to the laser path. Only a very thin sheet, cut through the spray, is imaged with planar sheet imaging where as the whole spray is imaged in line of sight imaging. As shown in Figure 5(a), the concept of ballistic imaging relies on differing propagation times for photons that pass through the spray without alteration (ballistic), and those that undergo significant scattering, refraction, or diffraction (diffuse). The former will maintain their direction of propagation, phase, and polarization and can be preferentially selected in a number of ways. It is possible to use a spatial filter or polarization gating to reduce the contribution from diffuse photons that exit at large solid angles (2, 31). However, this does not provide sufficient discrimination for image-contrast enhancement in dense regions of the spray as not enough diffuse photons are rejected. It is

also possible to use coherence gating, such as second harmonic generation, where the imaging beam emanating from the spray is passed through a non-linear crystal. In this case only those photons that pass through the spray without scattering will remain coherent and be frequency shifted through the crystal to be imaged onto the camera. This approach is commonly used in other dense media, such as biological tissue, where the level of multiple scattering is very high. However, this approach is too restrictive in that it eliminates even forward scattered photons that could still be used for imaging. Hence, coherent gating does not allow enough photons for single-shot imaging. Since multiply scattered photons have a longer path length and have longer propagation times through the spray, an alternative is to separate photons through time gating. The approximate time separation for photons with an increased path length of 1 mm is approximately 3.33 ps. Hence, a short pulse laser source (sub-picosecond) will undergo temporal stretching as it propagates through the spray, as shown in Figure 5(a) (right), where ballistic photons exit earliest in time and diffuse photons exit later and over a longer period of time. Ultrafast time gating on the order of picoseconds provides an intermediate level of discrimination, allowing photons with little or no deviation from the original path to be used for high-contrast, single-shot imaging of liquid core structures within the spray. Only photons that undergo significant deviation from their original path will emerge later in time and be rejected (32).

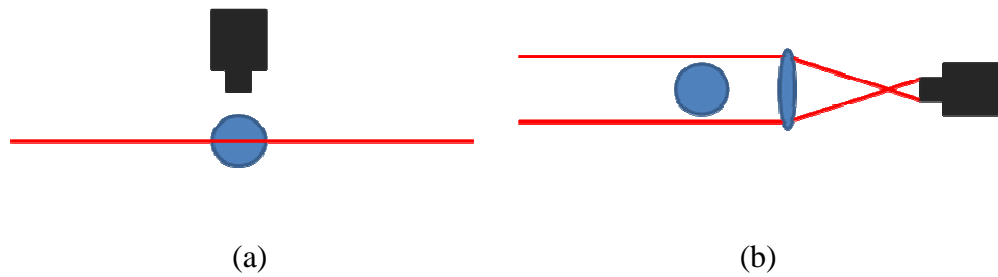


Figure 4. Typical imaging modes including planar sheet imaging (a) and line sight imaging (b).

The optical components for the ballistic-imaging system utilized in this effort are modified from a previous design used for Diesel sprays (23) and gas-turbine augmentor sprays (1, 24). As shown in Figure 5(b), a 1-Watt, 1-kHz ultrafast (~ 80 -fs pulsewidth) laser is split into an imaging beam and a gating beam using a waveplate (WP) and thin-film polarizer (TFP) combination. The energy ratio between each beam is typically 10:90, respectively, and can be continuously varied to optimize image quality for different magnifications and optical densities (33).

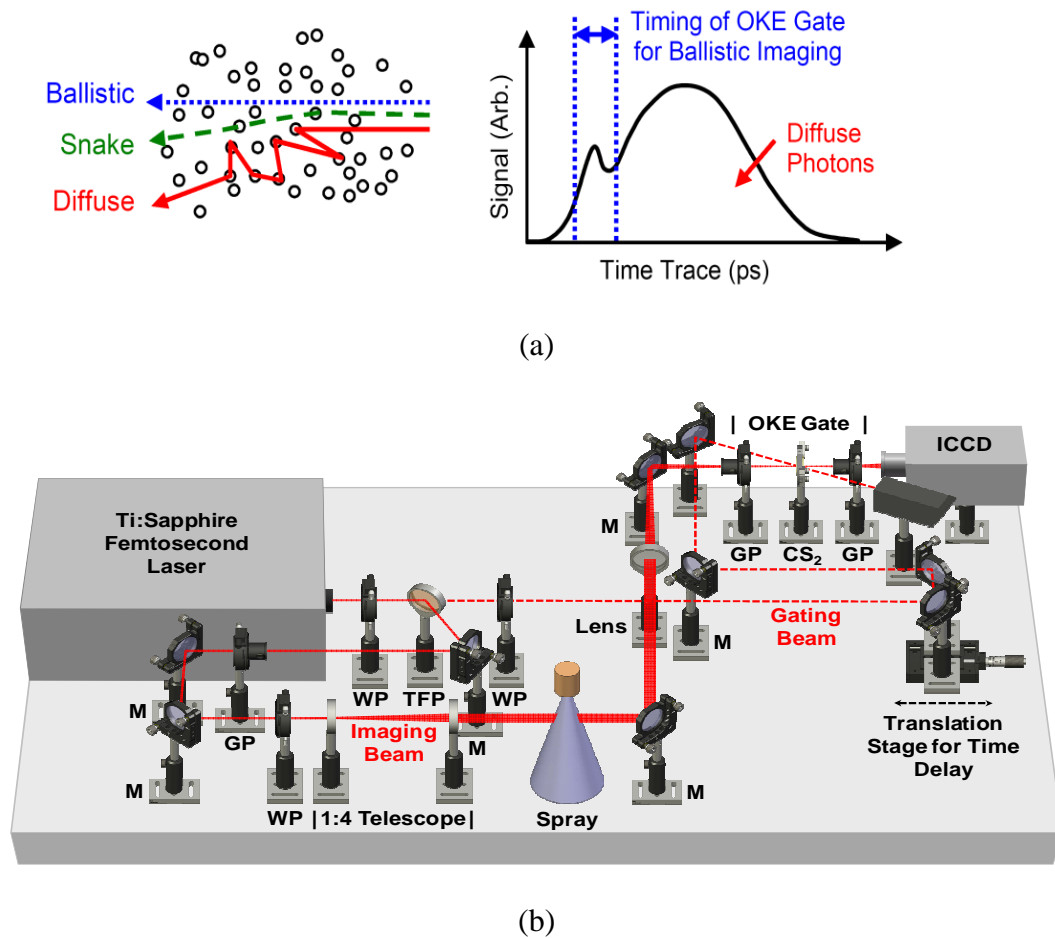


Figure 5. (a) Ballistic imaging concept showing photon path of ballistic, snake, and diffuse light (left) and conceptual time trace of photons exiting the spray (right). (b) Schematic of ballistic-imaging system. Symbols: WP – waveplate, TFP – thin film polarizer, GP – Glan laser polarizer, M – mirror, OKE – optical Kerr effect, CS₂ – carbon disulfide, ICCD – intensified charge-coupled device camera.

At low levels of imaging beam energy, a Glan laser polarizer (GP) is required to ensure that a linear polarization is maintained. A half-wave plate is then used to select the imaging beam polarization for optimization during the experiment. After a 1:4 telescope, the ~25 mm beam passes through the spray and is focused into the OKE time gate consisting of a carbon disulfide (CS₂) cell between crossed Glan-laser polarizers. When struck by the gating

beam, a short-lived birefringence is induced in the CS₂ for about two picoseconds, rotating the polarization of the imaging beam and allowing it to pass through the second polarizer of the OKE time gate for detection (28-30) by an 1024 × 1024 pixel, 16 bit intensified charge-coupled device (ICCD) camera. The angle between the gating beam and imaging beam is minimized to ensure uniform time gating across the image. Only the central ~15 mm of the beam is collected onto the ICCD, overfilling the detector and improving signal uniformity. The timing between the imaging beam and gating beam is controlled with a physical delay line that allows preferential detection of ballistic and near-ballistic photons using a micrometer-driven translation stage. Time delays of tens of picoseconds are possible with a resolution of 33 fs.

The increased field-of-view of the current system enables low-distortion imaging for nozzle sizes of ~5-10 mm and differs somewhat from previous ballistic-imaging systems used for studying liquid injection holes ~1-2 mm in diameter. To help maintain sufficient signal levels, the diffuser screen used in previous efforts to form the image was eliminated and the beam is imaged directly onto the ICCD front window. To reduce geometric aberrations and sources of birefringence in the OKE time gate, only a single, 50-mm-diameter, long-focal-length lens is used for (a) focusing the imaging beam through the OKE time gate, (b) soft spatial filtering, and (c) imaging onto the detector (34).

2.2 Nozzle Set-Up

Measurements are performed with air and water as the test fluids in a swirl-coaxial rocket injector with a typical geometry as shown in Figure 6. This nozzle, was described conceptually in Section 1.1.

An overview of the injector design and operation is found in previous articles (35-36) and is briefly summarized here. Gaseous air enters into a small settling chamber and feeds the inner diameter of a modular nozzle section. Water enters from a side port, travels along an annular passage surrounding the nozzle, and is injected into the inner diameter of the nozzle through small holes with swirling trajectories. The geometry near the nozzle exit is shown in Figure 7, with features listed in Table 1. The liquid forms a film along the inner surface and is atomized through shearing action at the exit lip of the nozzle tip. Various exit passage geometries and diameters were tested, as illustrated in Figure 7. Injector A and B have the same air passage diameter (5.4 mm) and number of liquid injector holes (4), but the exit flow area of Injector B is twice that of Injector A. In addition, Injector A has a recessed cavity whereas Injector B has a sudden expansion. Injector B and C have similar geometries, but Injector C has larger passage diameters and only 3 liquid injection holes. Likewise, Injector A and F have similar geometries, but Injector F has larger passage diameters. Injector D is a special case of a converging air passage at the nozzle exit, and Injector E is a special case of a sudden expansion with a shrouded liquid injection geometry.

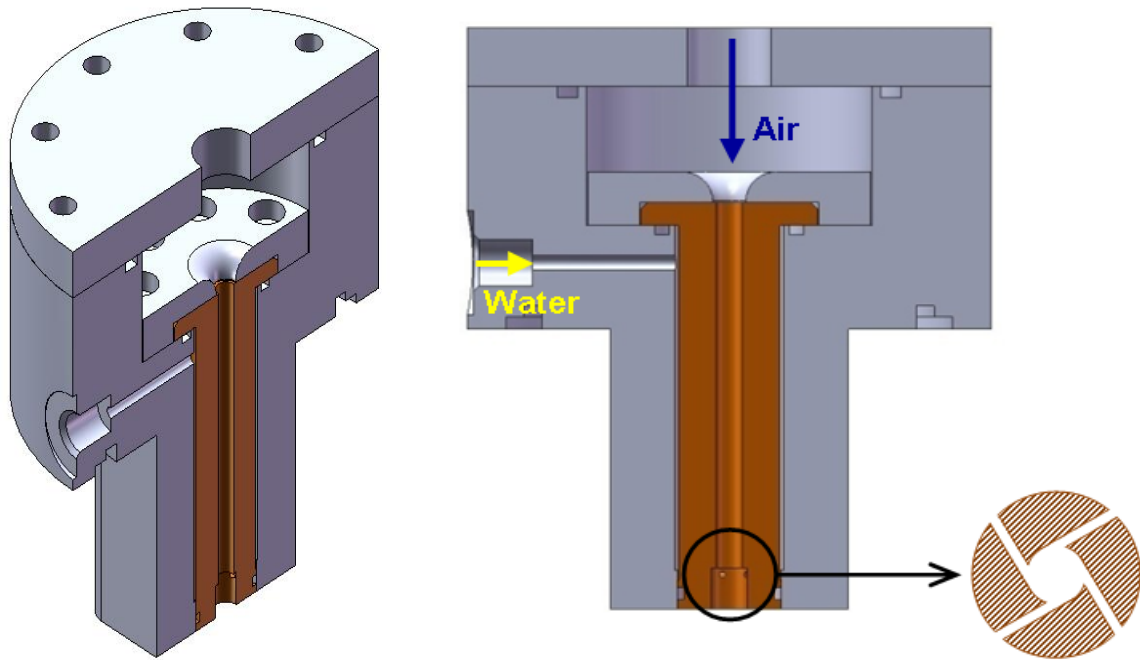


Figure 6. Swirl-coaxial liquid rocket injector.

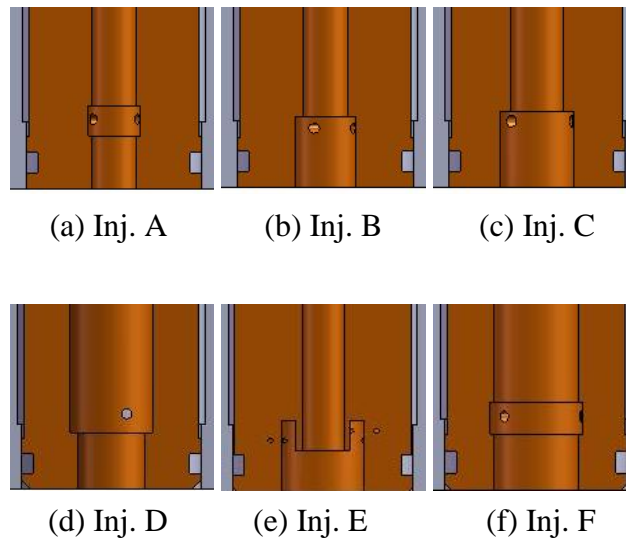


Figure 7. Injector nozzles with exit diameters of (a) 5.4 mm, (b) 7.6 mm, (c) 9.1 mm, (d) 8.1 mm, (e) 10.2 mm, and (f) 10 mm.

Water flow rates were varied from 0.8 to 2.6 liters per minute (lpm) using a 3.8-lpm liquid rotameter with +/-2% full scale accuracy, and the central air flow was varied from 200-570 lpm with a 570-lpm air rotameter with +/-2% full-scale accuracy. These conditions, listed in Table 2, resulted in hollow-cone liquid sprays with varying cone angles, breakup lengths, and atomization regimes. Light attenuation levels were measured for reference with a continuous-wave HeNe laser source varied from 97% to 99% across the spray for many of the conditions presented here. This means that the percentage of original light (I_0) that exits the spray (I) in the beam direction is about 1% to 3%, and that the rest of the light is scattered off-axis. This light attenuation in the spray corresponds to optical densities $OD = \log_{10} (I_0/I) \sim 1.5$ to 2. On a natural log scale, this would correspond to absorbencies of $A = \ln (I_0/I) \sim 3$ to 5.

Injector	Exit Dia. (mm)	Passage Dia. (mm)	No. of Water Passages
A	5.4	5.4	4
B	7.6	5.4	4
C	9.1	6.5	3
D	8.1	10.1	3
E	10.2	4.9	10
F	10	10	3

Table 1. Rocket injector design parameters.

Inj	Air Flow (lpm)	Water Flow (lpm)
A	200-340	0.8-2.6
B	250-410	0.8-2.6
C	460-570	0.8-2.6
D	200-460	0.8-2.6
E	200-260	0.8-2.6
F	430-570	0.8-2.6

Table 2. Flow conditions.

For all injectors and flow rates the spray exits into an atmospheric-pressure test chamber that was purged to remove the build-up of mist. Optical access was provided just

below the nozzle exit to track primary breakup. Optical access consisted of openings in the spray chamber walls and did not employ windows in order to avoid mist build up and possible effects of birefringence inherent in glass supplies. This open optical access allowed the best possible imaging with the least amount of variations.

CHAPTER 3. IMAGE PROCESSING

Using an ICCD camera, data was collected for each nozzle using both ballistic imaging and shadowgraphy techniques. After collection, raw data was processed using background subtraction and image normalization to enable comparisons between various operating conditions throughout the testing process (24). Images are normalized to eliminate variations in the image that occur during acquisition and do not pertain to the object being imaged. Variations in the image can include room light, spurious laser scattering, spatial laser intensity variations, variations in time gating across the image in the optical Kerr effect time gate, day to day fluctuations in laser power, and other background noise based on camera gain settings. By eliminating variations the intent is to obtain a standard image without any non-relevant elements being contributed from the specific conditions in which the image is acquired. Removing variations from an image improves the definition of the image and aids in feature recognition. A normalized image is given by $NI = (SI-R)/(NSI-R)$, where SI is an image of a spray, NSI is an image of no spray, and R is the background room light.

Image normalization is also necessary to enable quantitative comparisons between data sets with and without time gating. For example, the OKE time gate reduces the available laser energy by about a factor of three as compared with non-time-gated shadowgraphy. A set of 96 images is collected for each flow condition to enable statistical analyses, such as ensemble means and probability density functions (PDF's). Ensemble means represent the average normalized signal for the full ensemble of images collected at a

particular point in the flow, while PDF's represent histograms collected for the same point in the flow, normalized such that the area under each PDF is unity. Since the signal is normalized to the reference light intensity, the optical density is found from $OD = -\log_{10}(\text{normalized signal})$. A normalized image is compared with an image which has not been normalized in Figure 8.

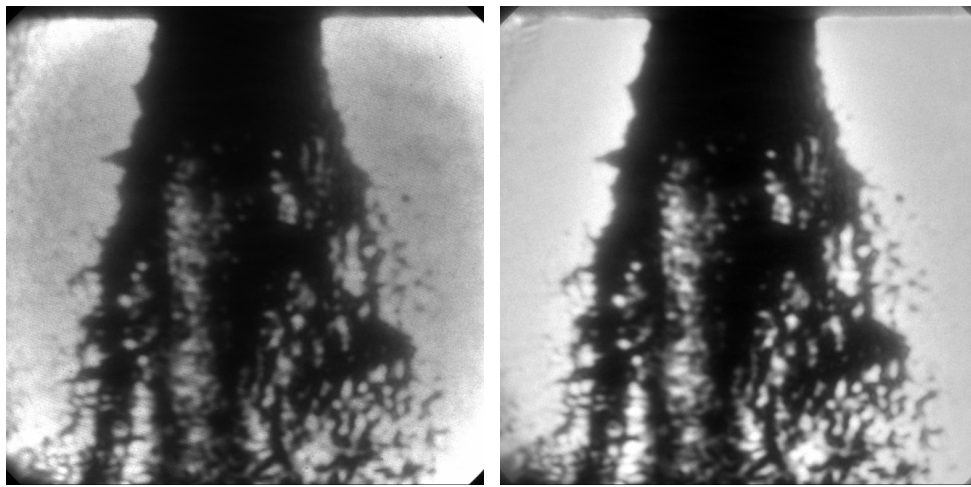


Figure 8. Non-Normalized (left) and Normalized (right) Ballistic Images for Injector A.

Viewing the image on the left in Figure 8 there is considerable noise present compared to the image on the right. Light leakage is visible around the edges of the frame and scattering is present in the area around the spray. Once the image has been normalized the background becomes smooth and areas where no spray is present become brighter. While this type of normalization does not sharpen the image, it does improve the contrast between areas of structure and areas of no structure. With improved contrast, liquid breakup and atomization can be identified with more ease.

CHAPTER 4. RESULTS

All experiments were performed at atmospheric pressure. Data was collected in sets of 96 image using ballistic imaging and shadowgraphy. Images were centered 10 mm down from the nozzle exit and normalized as described earlier. The gray scale varies from 5% to 95% of the range of intensity values found in the images. A variety of break-up mechanisms are apparent in the ballistic images that are not apparent in the shadowgraphs and are discussed in this section. Unfortunately, the path-averaged nature of these measurement techniques limits the analyses to qualitative features. Nonetheless, the nature of the breakup process and the state of liquid atomization can be used to select appropriate spray models, and assumptions regarding initial conditions can be adjusted to improve model accuracy. After discussions regarding data from specific rocket injectors, implications for signal to noise and contrast improvement utilizing time gating are discussed.

4.1 Injector A

Figure 9 shows ballistic images and shadowgraphs for Injector A and allows direct comparison of the two imaging techniques. The ballistic images clearly show fluid columns that extend from the nozzle exit and through the entire viewing area. These separate columns become less apparent as the water flow is increased. Atomized droplets located around the fluid columns are not visible in the ballistic images because the time gate preferentially allows photons that pass more or less straight through the spray. Hence, the normalized images of ballistic photons will show regions of dense droplets as voids in the spray.

However, it is clear from the shadowgraph images that the regions that appear as voids in the ballistic images are filled by an attenuating liquid field.

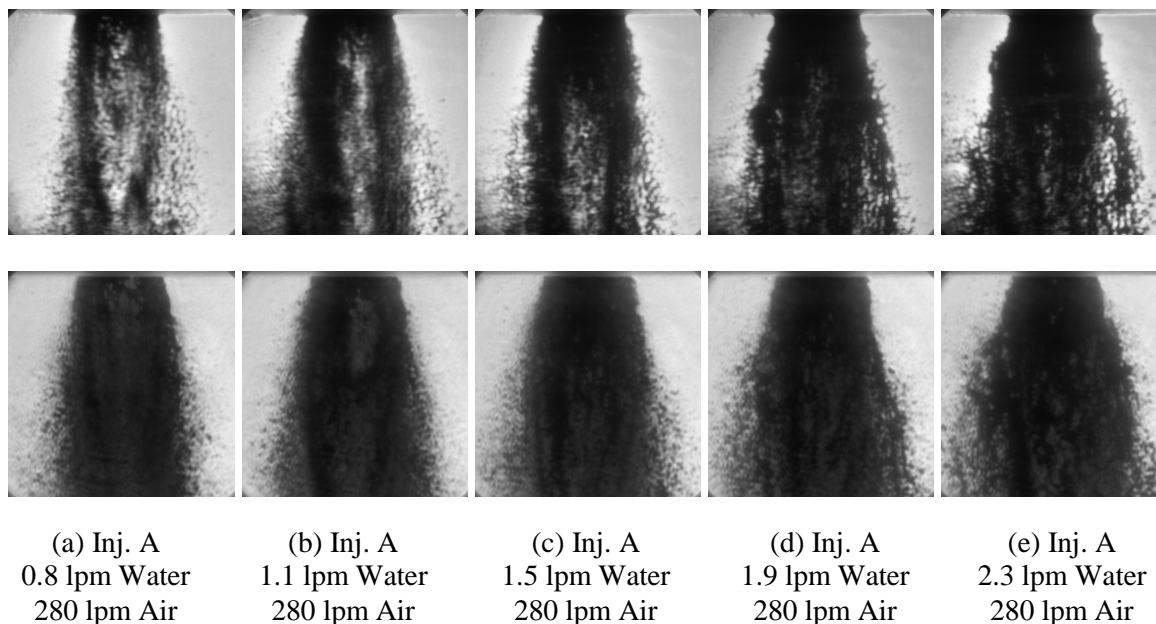


Figure 9. Ballistic images (top row) and ultrafast shadowgraph images (bottom row) for Injector A.

Figure 9 includes a series of single-shot images just below the exit of the rocket injector for a variety of flow conditions. The air flow rate is fixed at 280 lpm and the water flow rate increases from 0.8 lpm to 2.3 lpm from left to right. While the spray pattern at each flow condition varies from shot to shot, each of the images in Figure 6 is fairly typical at each flow condition and provides an accurate representation of the flow structure. At the lowest flow rate of 0.8 lpm, the spray shown in Figure 9(a) has a non-uniform distribution throughout the field of view and appears as distinct liquid columns with small fluid fragments surrounding them. At an increased liquid flow rate of 1.1 lpm, the fluid columns

continue to increase in size and density. At the higher liquid flow rate of 1.5 lpm, shown in Figure 9(c), the larger optically dense flow regions begin to form thinner, more elongated structures. In addition, the location where these liquid columns begin to form moves further downstream, and a core-like structure begins to form near the nozzle exit. It is not clear from these images whether this optically dense apparent liquid core is composed of a solid cone or a hollow cone. These trends continue at higher liquid flow rates, as shown for 1.9 lpm in Figure 9(d). When the water flow rate is increased to 2.3 lpm, as shown in Figure 6(e), the apparent core becomes wider and more optically dense, the liquid-core breakup moves further downstream, and the larger liquid columns appear to have completely broken up into long, thin ligaments. The trends described from the ballistic imaging data are also present in the non-time-gated shadowgrams of Figure 9, although the internal spray structure is less clear. In fact, without the ballistic imaging data, the trends described above would be difficult to deduce. As described earlier, these shadowgrams are collected without a time gate so that the signal is composed of ballistic photons as well as diffuse photons from droplet scattering. Furthermore, it is possible to deduce the state of atomization more accurately by comparing data with and without the OKE time gate. The regions of the spray that appear to contain no liquid matter in the ballistic images of Figure 9 show the appearance of liquid matter in the shadowgrams of Figure 9. These regions are likely composed of small, atomized droplets that cause diffuse light scattering. Regions in which light is blocked in both ballistic images and shadowgrams likely indicate the presence of large-scale liquid structures or perhaps the presence of a liquid core. These features with large-scale liquid structures are suggestive of a mixed regime of wind-induced breakup and atomization from strong shear forces.

It is apparent in the images that the ultrafast time gate improves contrast between regions that are composed of droplets and those that are composed of continuous-phase liquid. Further analysis of this contrast improvement is included after discussions about other injector geometries.

4.2 Injector B

Ballistic images are compared to shadowgraphs for Injector B in Figure 10. Much like Injector A, liquid core structures span the entire length of the viewing area. The process of secondary breakup is also apparent in these images, with intermediate-scale ligaments and fluid fragments appearing one nozzle diameter downstream of the injector exit. Once again the presence of atomized droplets surrounding the liquid core structures is not discernable from the ballistic images as these regions appear as voids, but light attenuation from a droplet cloud is apparent in the shadowgraph images. Hence, these images show even more clearly than for Injector A that the use of both ballistic and shadowgraph imaging provides information on the state of liquid breakup and atomization within the spray. While ballistic imaging shows the continuous liquid phase, it may lead to confusion if used without shadowgraphy, as the composition of the apparent voids would not be known. The shadowgrams, which result from the attenuation due to both the continuous liquid phase and the dense field of droplets, show that these apparent voids have liquid matter present. Due to the photophysics involved in both techniques, it is expected that the difference in the two images provides a qualitative description of the atomized phase. In future work, it would be advantageous to collect the ballistic images and shadowgrams simultaneously for shot to shot comparisons of images from both techniques.

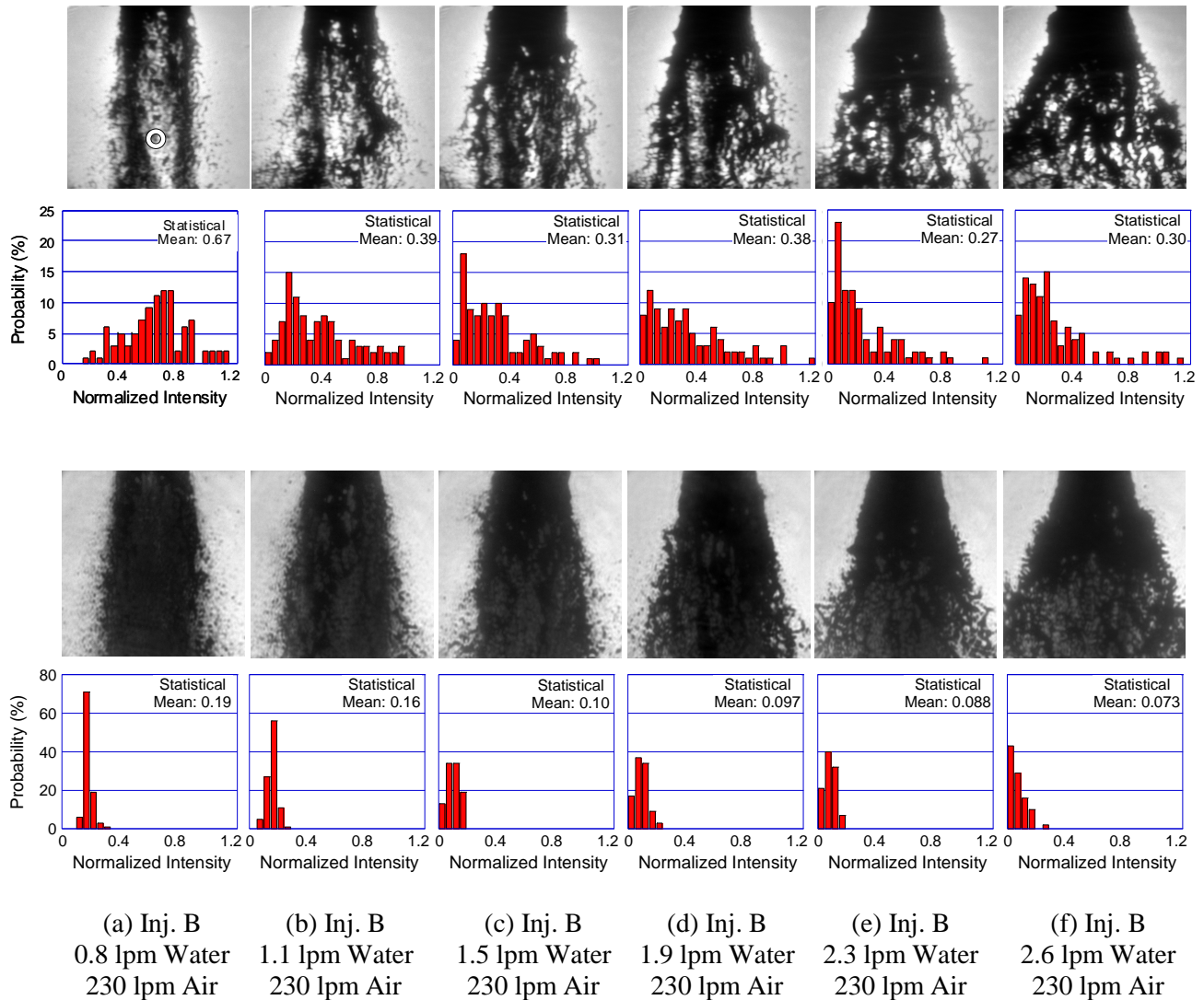


Figure 10. Ballistic images (top row), ultrafast shadowgraph images (bottom row), and corresponding PDF's for Injector A. Symbol © designates location for statistical analyses, two nozzle diameters downstream of nozzle exit.

Figure 10 includes a series of single-shot images just below the exit of the rocket injector for a variety of flow conditions. In this case, probability density functions from an ensemble of 96 images collected for each condition are also shown in Figure 10 for an

interrogation point that is ~ 2 nozzle diameters downstream of the nozzle exit plane. The air flow rate is fixed at 230 lpm and the water flow rate increases from 0.8 lpm to 2.6 lpm from left to right. As with all the data sets there is some variation in the spray pattern from shot to shot at each flow condition. The images in Figure 10 are fairly typical and provide an accurate representation of changes in the global spray structure as a function of flow condition. At the lowest flow rate of 0.8 lpm, the spray shown in Figure 10(a) has a non-uniform distribution throughout the field of view. As with Injector A, distinct columns of liquid appear to emanate from the rocket nozzle, and there does not appear to be a liquid core appearing near the nozzle exit. The PDF at the interrogation region shown in Figure 10(a) for this condition is somewhat Gaussian, and the ensemble average or statistical mean of 0.67 is close to the peak of the PDF at a normalized signal of 0.725. The fact that the peak probability is close to the statistical mean is indicative of the fairly symmetric PDF distribution and suggests that spray structures passing through the interrogation region are fairly random at this point in the flow for this flow condition. This due to the fact that this point in the flow is not traversed by large-scale, continuous-phase liquid structures. It is interesting to note that the long columns do not randomly cross towards the center of the viewing area, indicating that there may be a driving influence for this particular flow pattern. It may also be deduced that the spray may be a hollow core and that the darker regions on the exterior are simply the result of a longer path length of continuous phase liquid on the edges as compared to the center. This may be intuitive from the geometry of the nozzle, which places the liquid film at the edges of the spray and the driving air flow at the center. However, it is also possible that these columns are distinct structures that tend to occupy the exterior of the spray rather than the edges of an axisymmetric hollow-cone structure. More

evidence for the actual spray structure will become clear upon further analysis of other injectors and the influence of the internal nozzle liquid flow pattern on the spray exiting the nozzle.

Meanwhile, the data in Figures 10(b) to (f) suggest that the spray consists of distinct elements indicative of long ligaments with strong light attenuation. These ligaments seem to be highly perturbed by strong shear forces as well as transverse velocity components. As shown at the liquid flow rate of 1.1 lpm, there is an increase in the occurrence of thin, elongated liquid columns that span nearly the entire length of the image, as well as increased randomness in the shape of the structures. When the liquid flow rate increases to 1.5 lpm, shown in Figure 10(c), the thin liquid columns become unstable, with additional thin structures appearing at a liquid flow rate of 1.9 lpm, as shown in Figure 10(d). These structures propagate into the interrogation region, leading to an increased probability of observing lower signal intensities. Hence, the PDF's shown in Figure 10(b) to Figure 10(d) become increasingly asymmetric and shift to lower values at higher flow rates because of significant light attenuation occurring with the passage of optically dense liquid structures.

When the water flow rate is increased to 2.3 and 2.6 lpm, as shown in Figures 10(e) and 10(f), the location of liquid-core breakup moves further downstream as the liquid-to-air momentum ratio increases. This leads to the appearance of two distinct regions of the flow, including an initial region of high optical density near the injector exit, appearing as an apparent liquid core, followed by a region with a sudden increase in cone angle and a series of thin liquid strands. The increased level of asymmetry in the PDF's with increased flowrate, as shown from Figure 10(a) to Figure 10(f), reflects a change in spray behavior at

the interrogation region from one that is dominated by more randomly occurring structures passing through the region to a spray pattern dominated by large-scale organized structures.

The trends from the ballistic imaging data are also present in the non-time-gated shadowgrams of Figure 10, with the internal spray structure again being less clear. Once normalized, the resulting shadowgrams have a higher, more uniform optical density. This dark appearance is accompanied by PDF's with much narrower intensity distributions, presumably because the signals are more consistently attenuated regardless of the state of atomization. In contrast, images collected with the OKE time gate are comprised preferentially of ballistic photons, which are not scattered by the dense spray. After normalization, this time gating results in a lower apparent optical density in regions of the spray composed mostly of small droplets. As a measure of contrast ratio, peak signals within apparent gaps in the spray compared with signals in regions consisting of liquid-core structures are about 10:1 in ballistic images and about 3:2 in non-time-gated shadowgrams. The overall effect of ballistic imaging, therefore, is the ability to show higher apparent beam penetration in dense, atomized regions of the spray, with an image contrast enhancement of ~6.6:1. This allows improved characterization of highly heterogeneous polydisperse sprays. The significant increase in image contrast for the moderately dense environment (optical density ~1.5 to 2.0) studied here is somewhat surprising and may be attributable to the relatively large spatial extent of the droplet field, which increases the time of flight for multiple scattered photons and enhances the ability to isolate ballistic and snake photons.

Comparing data with and without the OKE time gate makes it possible to surmise the state of break up and atomization more accurately. As with Injector A, these regions are likely composed of small, atomized droplets that cause diffuse light scattering. Regions in

which light is blocked in both ballistic images and shadowgrams likely indicate the presence of large-scale liquid structures or perhaps the presence of a liquid core. Regions filled with atomized droplets seem to occur primarily in the interior of the spray, so it is possible from this analysis to surmise the overall spray structure. The classical hollow cone spray has a dense field of droplets in the outer region of the spray and relatively few droplets in the center. The spray described here is analogous but with liquid sheets and strands that form the exterior boundary of the spray cone and significant levels of atomization within the interior where the air flow is highest.

Figure 11, shown below, in which the statistical mean and standard deviation of the signals are plotted versus liquid flow rate at the interrogation region corresponding to that of Figure 10, helps to illustrate the increased sensitivity of ballistic imaging to the heterogeneous nature of the spray. These data were collected by measuring the variation of signal intensity from image to image at a point two nozzle diameters downstream from the nozzle exit lip.

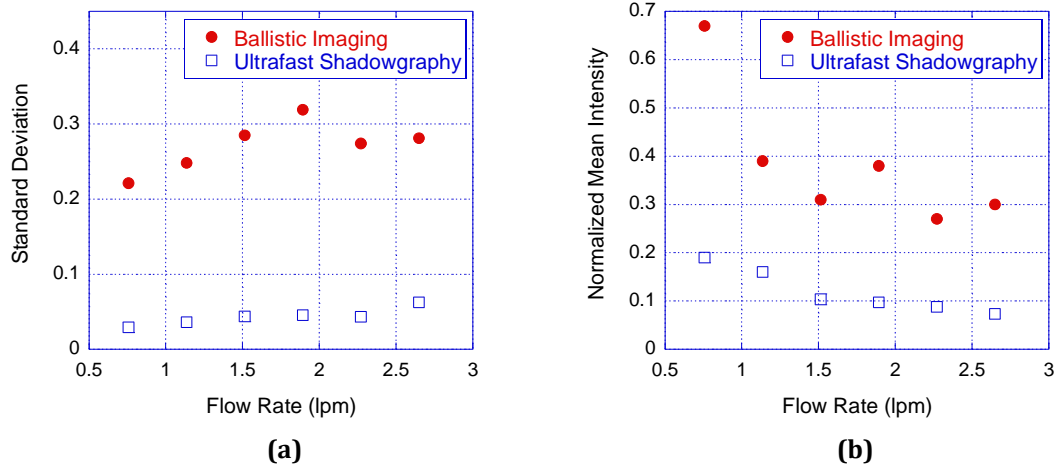


Figure 11. (a) Normalized mean intensity and (b) standard deviation as function of water flow rate for both ballistic imaging and ultrafast shadowgraphy. Data collected two nozzle diameters downstream of nozzle exit.

The statistical mean and standard deviation of signal intensities for the ballistic images are much higher than those of the non-time-gated shadowgrams. While the trends are similar for both techniques, the relative change of signal intensity and standard deviation is greater for the ballistic images. The shot-to-shot standard deviation of normalized images in Figure 11(b) increases as flow rate increases, which indicates that the relative signal contrast or frequency of occurrence between organized liquid structures and regions composed of smaller droplets is increasing. The shot-to-shot standard deviation reaches a peak and begins to drop at higher flowrates as the increased presence of organized liquid structures reduces the frequency of voids within the spray. The relative signal and especially the shot to shot standard deviation provide a more quantitative measure of the ability of time-gated ballistic imaging to penetrate optically dense sprays.

While the flow conditions are changed, similar observations can be made regarding the spray structure of Injector B for different air and water flow rates, as shown in Figure 12. For the flow condition listed in Figure 12(a), the liquid structures are dominated by highly turbulent, intermediate-scale structures that are clearly undergoing significant secondary breakup. Increasing the air flow with the same water flow rate reduces the size and spatial extent of the intermediate structures and produces what appear to be three primary columns of fluid in the top of Figure 12(b). This is a dramatic change in flow structure that is not easily detected in the shadowgrams (bottom), and is somewhat counterintuitive. Based on the classical understanding of breakup regimes, described in Figure 1, it may be expected that the increased air flow would increase secondary breakup and reduce the size of liquid structures. This implies that the air flow may be fundamentally changing the characteristics of the liquid film that forms within the inner diameter of the rocket nozzle, perhaps reducing the residence time within the nozzle and leading to a non-uniform film vis-à-vis the finite number of liquid injection holes. While there are four liquid injection holes within the nozzle, as listed in Table 1, only three liquid columns would be visible given the nozzle orientation shown in Figure 6. This trend is confirmed when the water flow rate is increased, as shown in Figure 12(c). The increased water flow rate would result in a higher tangential velocity and perhaps a more uniform liquid film. The result is a much different flow field from either of the cases shown in Figures 12(a) and (b). An apparent liquid core begins to appear near the nozzle exit, followed by break up into long ligaments that are oriented with the flow. Given the spreading angle of the overall spray, it is likely that these ligaments are also propagating with some radial velocity. In this case, the number of liquid columns does

not seem to be related to the number of injection holes and the spray seems to have lost the “memory” of the interior nozzle flow. Interestingly, the spray structure is similar to that of Figure 10(c), which has a similar ratio of liquid to air flow rate as Figure 12(c). This implies that there is an effect of air to liquid momentum flux ratio that may characterize the behavior of the interior nozzle flow and resulting exterior spray. These observations have lead to a more rigorous study of the details of the interior flow, which is the subject of ongoing work and is beyond the scope of this thesis.

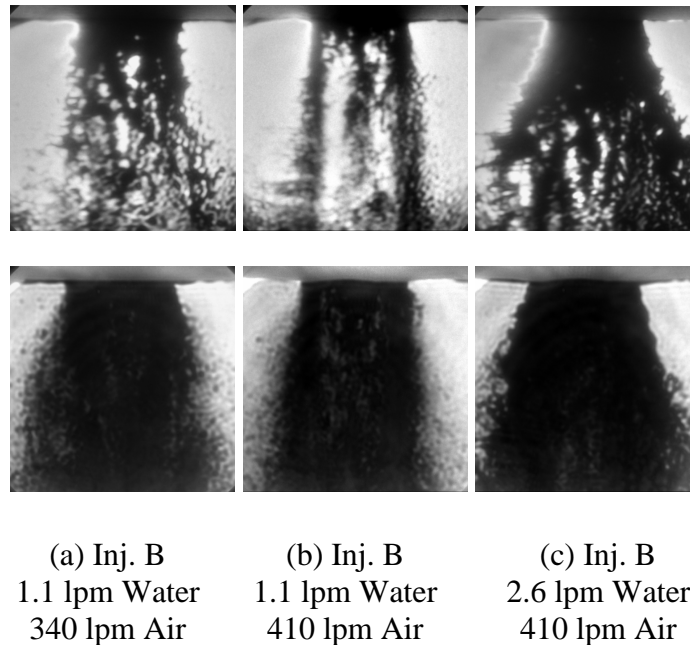


Figure 12. Ballistic images (top row) and ultrafast shadowgraph images (bottom row) for Injector B.

Nonetheless, the more definitively illustrate the effect of the interior flow pattern within the injector, the viewing orientation of the spray nozzle was rotated so that only two main liquid columns would appear for the same condition as illustrated in Figure 12(b). The

data for a series of single-shot images collected with and without rotation are shown in Figure 13, with the top row showing the original orientation of the rocket injector and the bottom row showing the new orientation. These images confirm that the liquid spray under these conditions can exhibit a “memory” of the initial conditions within the nozzle. This is an important feature that should be captured in successful modeling efforts. The three liquid columns appear as two columns for the rotated view of the bottom row, leading to a deceptively small spray diameter for these images. This effect can be detected by comparing ballistic imaging data at the two orientations, and illustrates the usefulness of utilizing time gating for photon discrimination. These data also provide evidence to support earlier descriptions of the spray structure under these conditions as having distinct liquid columns, like four legs on a stool, rather than the classical hollow-cone structure.

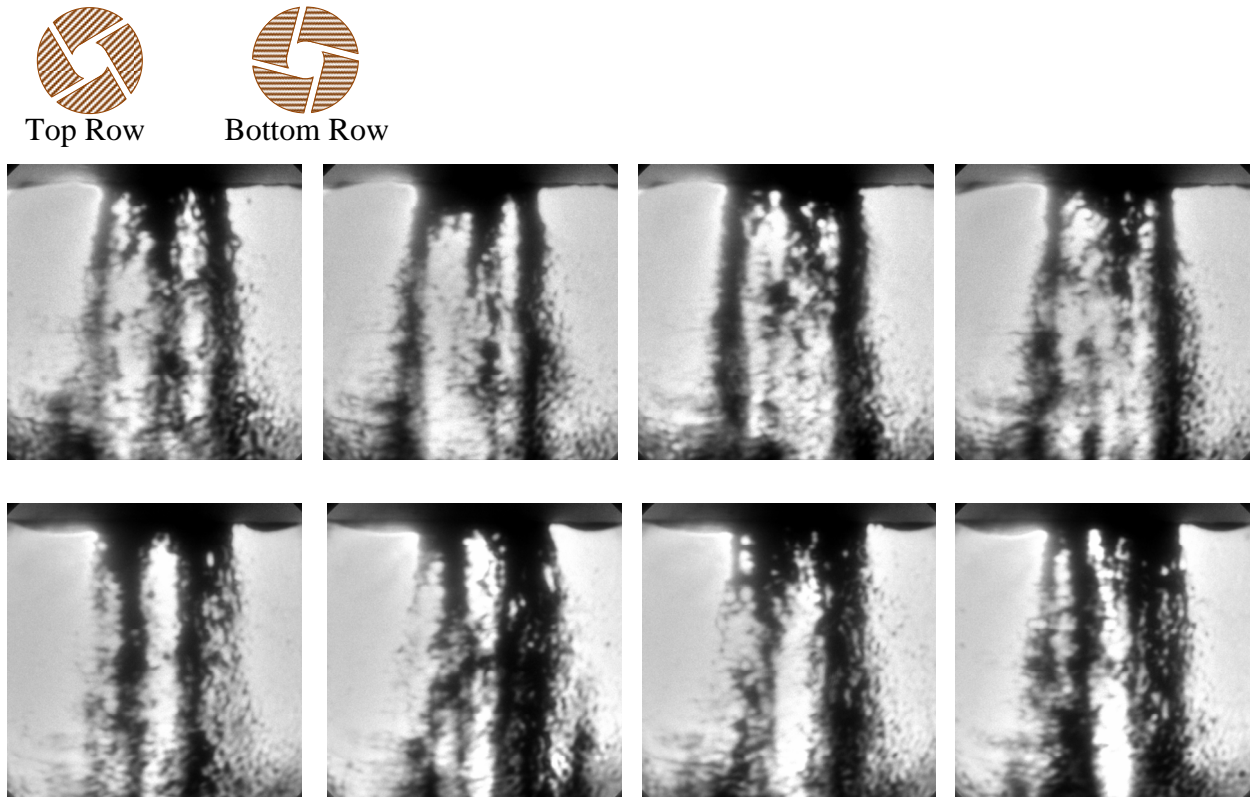


Figure 13. Ballistic images for Injector B at 1.1 lpm water and 410 lpm air. Top and bottom rows represent cases in which the injector has been rotated as indicated above.

4.3 Injector C

For Injector C, shown in Figure 14, the water flow was kept the same as for Figure 12(c), but the air flow was increased to maintain a similar velocity magnitude for both cases. These images were collected at the same flow condition to illustrate natural variations in flow structure. As with previous cases, comparison of ballistic and shadowgraph images clearly shows the presence of organized liquid structures along with a dense core of droplets between the structures. This is indicative of a mixed spray regime where wind induced

breakup is prominent throughout large regions of the spray and is accompanied by strong secondary breakup and atomization.

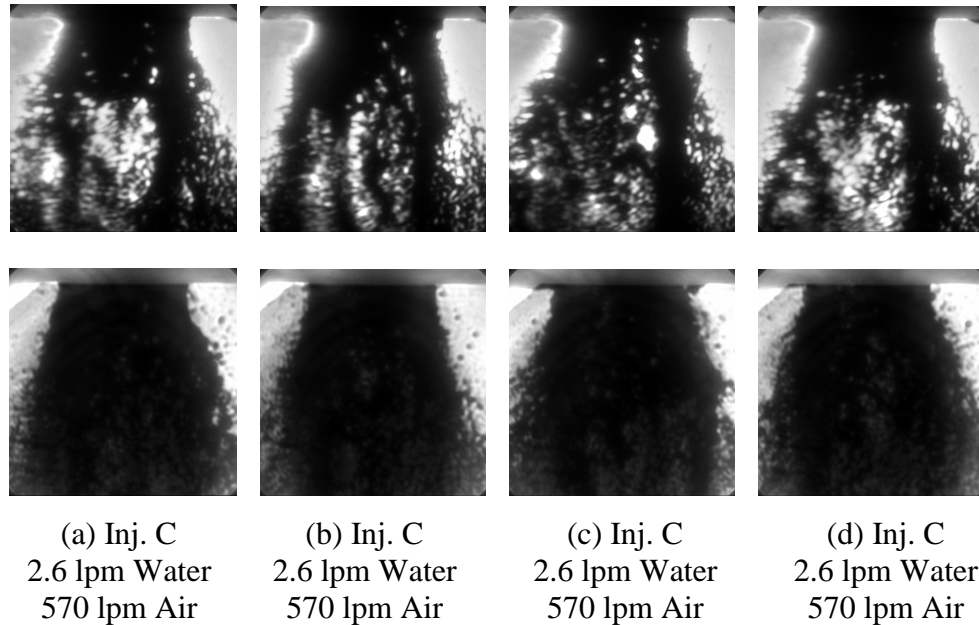


Figure 14. Ballistic images (top row) and ultrafast shadowgraph images (bottom row) for Injector C, showing a series of images at the same flow condition.

It is apparent that the flow is highly unsteady. Sprays similar to the ones imaged in Figure 14(a) occur most often in the data. However, the spray fluctuates and images like those of Figures 14(b), (c), and (d) also frequently occur in data sets. Despite variances in the spray formation, the liquid break up process remains generally the same. Injectors B and C both have sudden expansions at the nozzle exit, as shown in Figure 7, with injector C having both a larger passage diameter and exit diameter as listed in Table 1. Note that the water flow rates are equal in Figures 14 and 12(c), but the air flow rate in Figure 14 is increased to maintain a similar velocity magnitude. It is interesting to note that the liquid-core breakup occurs in a similar fashion for like injectors. Both injectors show two distinct

regions of flow. The first region of flow is directly after nozzle exit and is an area with a very high optical density in both ballistic images and shadowgrams. This area of high optical density in all images suggests that the liquid-sheet emanating from the nozzle is continuous, albeit with a hollow core. As the flow progresses away from the nozzle exit, breakup begins to occur. This is the second region of flow. The liquid-core breaks up into long liquid structures which span the rest of the frame. Fluid fragments and intermediate ligaments are also present but are only discernable in the ballistic images. The shadowgrams for the second region of flow show that the areas of high signal in the ballistic images are actually filled with a highly attenuating field. This occurs for both Injectors B and C. Using both ballistic imaging and shadowgraphy it is possible to discern that these injectors at equivalent flow rates break up in a very similar manner.

4.4 Injector D

Injector D is shown in Figure 15 and illustrates exceptionally well how ballistic imaging can help reveal the liquid-core breakup from an injector. Several samples are taken from the 96 image data set to show flow variations due to the highly unsteady flow. From this data set it would appear that there are dense optical structures spanning the length of the frame. The ballistic images for Injector D are shown in the top row of Figure 15, and shadowgrams are shown in the bottom. It is clear that liquid exiting the nozzle either is not formed into a continuous conical sheet or begins breaking up almost immediately.. Fluid structure is very sparse and consists of small ligaments and fluid fragments. These images bear significant similarity to the images in Figure 13 for Injector B. In fact, the exit

diameters for both injectors differ only slightly and the ratio of air to liquid flow rates are similar for both. The images shown in Figure 15 consistently show three liquid columns, likely corresponding to the three liquid injection holes for this nozzle design.

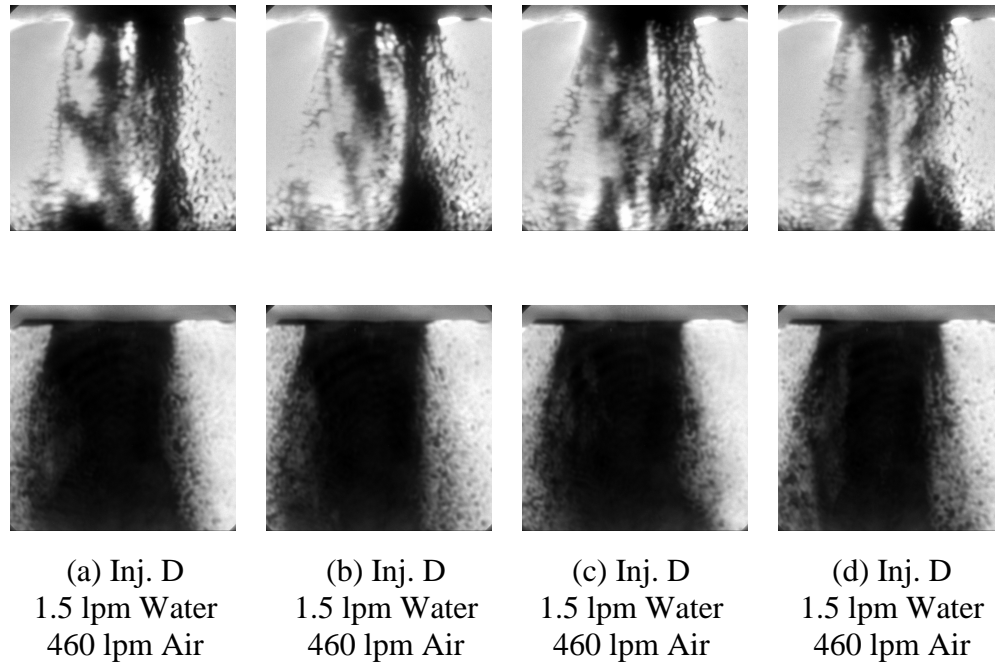


Figure 15. Ballistic images (top row) and ultrafast shadowgraph images (bottom row) for Injector D.

4.5 Injector E

Ballistic images and shadowgrams are shown for Injector E in Figure 16. The water flow rate was 1.5 lpm but the air flow rate was 260 lpm because of a small passage diameter. When looking at the shadowgrams for Injector E, it appears that there is no fluid mist but only small fluid fragments. This is evident from the prevalence of voids apparent in the

shadowgrams. However, there does still appear to be increased light penetration with the use of time gating, indicating that the apparent liquid structures in the shadowgrams may be undergoing atomization. Due to limitations on the air flow rate for this nozzle, it was not possible to test its behavior in the strong atomization regime.

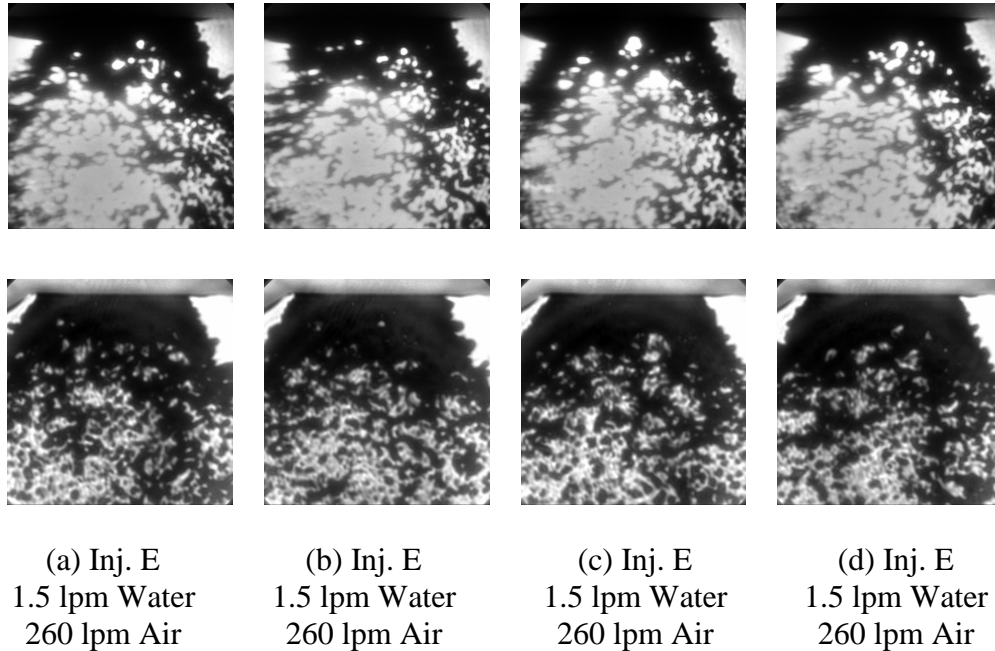


Figure 16. Ballistic images (top row) and ultrafast shadowgraph images (bottom row) for Injector E.

4.6 Injector F

Figure 17 shows ballistic images of Injector F for an air flow rate of 570 lpm. The water flow rate varies from 0.8 lpm to 2.6 lpm, as shown in Figures 17 (a) to (f). In Figures 17 (a) and (b) there is very little fluid structure. Only some small ligaments are present. As the water flow rate is increased for Figure 17 (c) it is apparent that there is some fluid “memory” from the liquid injection holes within the nozzle. This “memory” is made evident

by the two distinguishable columns that span the length of the frame. The water flow rate continues to increase for Figures 17 (d) to (f). The fluid columns disappear as the spray becomes optically dense. The optical density continues to increase as the water flow rate is increased. Shadowgrams were not collected for this condition, but many of the characteristics discussed earlier are also present in this spray

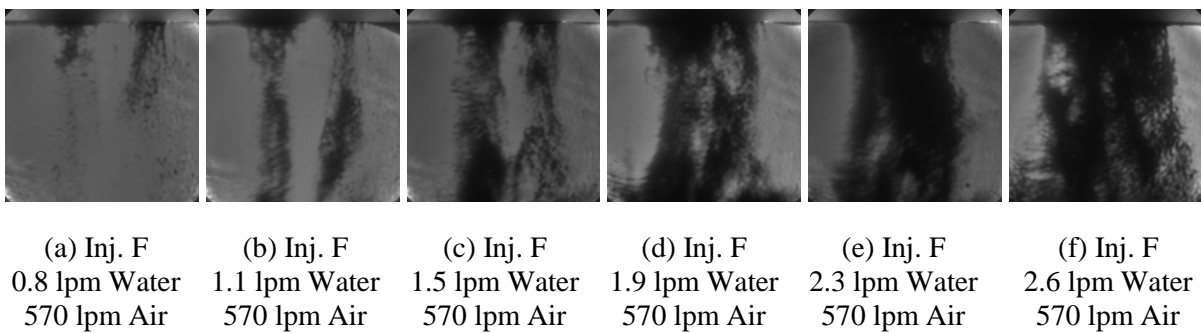
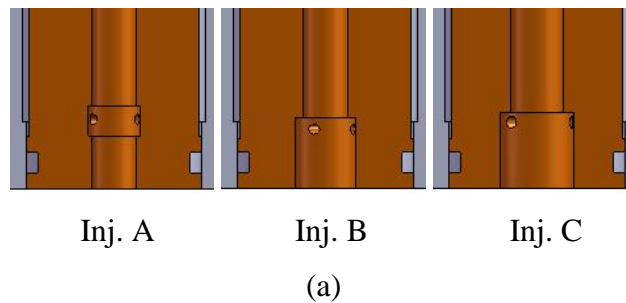


Figure 17. Ballistic images for Injector F.

4.7 Injector Comparison

In addition to the tests showing the differences of ballistic imaging and shadowgraphy, it is possible to compare the various rocket nozzle geometries. A subset of the nozzle shown in Figure 7 was used for this purpose, as shown in Figure 18 for convenience. The nozzles differ primarily by the size of the nozzle exit diameter. Two of these injectors have four liquid injection holes, and the third has three injection holes. Results of the ballistic imaging experiments are shown in Figure 19, where a matrix of water and air flow conditions were tested. It is noted that the air flow rates were selected so that the nozzle exit velocities from injectors A, B, and C were relatively constant. This allows comparison of

spray patterns for nozzles of differing size but comparable gas momentum. As shown in Figure 19, the data show similarities in spray angle for injectors A, B, and C under these conditions. There are some notable differences in the details of the breakup process as the liquid structures exit the nozzle, perhaps due to differences in liquid momentum as the nozzle diameter increases. The effect of increasing water flow for the same nozzle diameter and air flow (i.e., decreasing gas-to-liquid momentum ratio) is a dramatic increase in spreading rate. This is evident when comparing the top and bottom images. This trend is detected for all three nozzle configurations.



Injector	Exit Dia. (mm)	Passage Dia. (mm)	No. of Water Passages
A	5.4	5.4	4
B	7.6	5.4	4
C	9.1	6.5	3

(b)

Figure 18. Nozzle geometries used in previous ballistic imaging discussions. Nozzles are illustrated in (a) and relevant parameters are listed in (b).

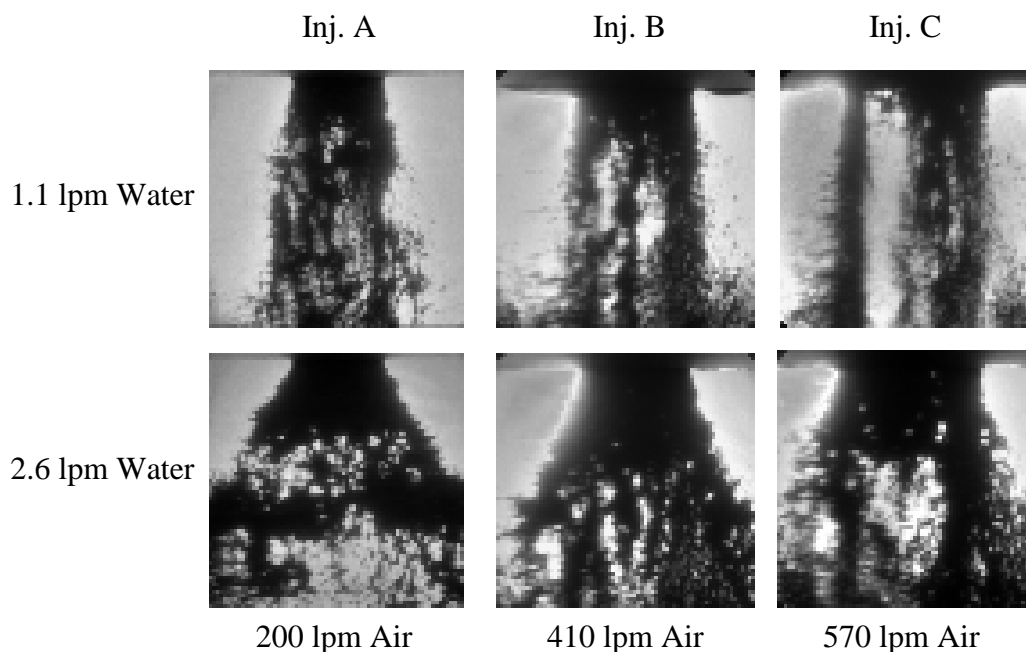


Figure 19. Ballistic imaging study of different nozzle injectors, where A, B, and C refer to geometries listed in Figure 18.

Keeping the water flow rate and the relative velocity of each nozzle relatively constant (i.e., comparing images left to right) shows some similarities in spreading angle, but the breakup process changes for the different nozzle configuration. This is likely due to the fact that the larger nozzle inner diameter from left to right would result in a reduced film thickness with increased non-uniformity. That is, it may be more difficult for the film to fill the inner diameter, leading to long liquid columns with “memory” of the liquid injection point within the nozzle. Indeed, as the nozzle diameter increases, the intermediate scale structures shown in Figure 19 for Injector A give way to long columns that span much of the spray for Injectors B and C.

The data in Figures 13 and 19 illustrate the potential importance of both nozzle geometry and momentum flux ratio on the liquid core break-up process in gas-centered swirl-coaxial rocket injectors. Based on the data shown previously in Figure 13, for example, it is believed that details of the liquid core break up process may be affected by the flow pattern within the injector nozzle. This internal flow pattern is affected by the air-liquid momentum flux ratio. As shown in Figure 20, as the air velocity is increased it has more of an effect on the spray angle and formation. At low momentum ratios the spray angle is very wide and is affected more by the tangential forces of the water. When the ratio increases to an intermediate level the cone angle decreases. The breakup remains similar to the low ratio as there is a dense region directly following the nozzle exit and fluid fragments further downstream. At high ratio levels the cone angle is once again narrow but fluid columns are formed from the nozzle exit. This is due to the high air velocities causing a non-uniform liquid film on the interior of the nozzle. These results imply that numerical models may need to capture the details of the interior nozzle flow for accurate predictions of rocket spray breakup. A modeling effort to accomplish this task is currently underway in collaboration with the current project.

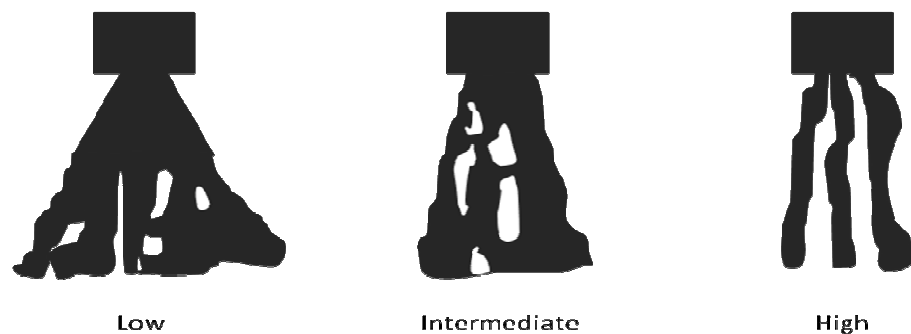


Figure 20. Breakup trends in air-liquid momentum flux ratio.

CHAPTER 5. SUMMARY AND DISCUSSION

The current work reports on the application of ballistic imaging for studies of rocket sprays with moderate optical density. It is clearly demonstrated that ballistic imaging can, under conditions where significant atomization is taking place, significantly enhance contrast ratio for visualizing liquid core dynamics in the interior of rocket sprays. Data from a number of different studies are summarized to show the effect of nozzle geometry and operating conditions on spray behavior. It is shown that the interior nozzle flow has a significant impact on the spray pattern. This was demonstrated by rotating the nozzle and showing changes in the spray pattern, as well as careful analysis of spray patterns under different conditions. Data at varying air and water flow rates show the effect of momentum flux ratio with regard to overall spray structure, detailed breakup phenomena, and liquid-core dynamics, which is valuable information for the development of predictive models. Hence, the use of time gating has been shown to be a powerful tool for extracting information on the internal spray structure of rocket sprays under optically dense conditions. Future work includes more detailed experiments within the nozzle itself to visualize the liquid film for various flow conditions, as well as collaboration with modelers to help in the development of predictive capability. Further work is also needed to test ballistic imaging under high pressure conditions.

BIBLIOGRAPHY

- [1] Linne, M.A., Paciaroni, M., Gord, J.R., and Meyer, T.R., "Ballistic Imaging of the Liquid Core for a Steady Jet in Crossflow," *Applied Optics* 44: 6627-6634 (2005).
- [2] Wu, P. K., Kirkendall, K.A., Fuller, R.P., and Nejad, A. S., "Breakup Processes of Liquid Jets in Subsonic Crossflows," *Journal of Propulsion and Power*, Vol. 13, 1997, pp. 64-73.
- [3] Wu, P. K., Kirkendall, K.A., Fuller, R.P., and Nejad, A. S., "Spray Structures of Liquid Jets Atomized in Subsonic Crossflows," *Journal of Propulsion and Power*, Vol. 14, 1998, pp. 173-182.
- [4] Sallam, K. A., Aalburg, C., and Faeth, G. M., "Primary Breakup of Round Nonturbulent Liquid Jets in Gaseous Crossflows," *16th Annual Conference on Liquid Atomization and Spray Systems*, ILASS, Monterey, CA, 2003.
- [5] Mayer, W. and Krulle, G., "Rocket Engine Coaxial Injector Liquid/Gas Interface Flow Phenomena," *Journal of Propulsion and Power*, Vol. 11, 1995, pp. 513-518.
- [6] Sallam, K.A., Aalburg, C., Faeth, G.M., Lin, K.-C., Carter, C.D., and Jackson, T.A., "Primary Breakup of Round Aerated-Liquid Jets in Supersonic Crossflows," *Atomization and Sprays* 16:657-672 (2006).
- [7] Miller, B., Sallam, K.A., Bingabr, M., Lin, K.-C., and Carter, C D., "Secondary Breakup of Aerated Liquid Jets in Subsonic Crossflow," AIAA Paper 2007-1342, 45th AIAA Aerospace Sciences Meeting, Jan. 2007.
- [8] Santangelo, P.J. and Sojka, P.E., "Focused Image Holography as a Dense Spray Diagnostic." *Applied Optics* 33:4132-4136 (1994).

- [9] Santangelo, P.J. and P.E. Sojka, "The Near Nozzle Structure of an Effervescent Atomizer Produced Spray," *Atomization and Sprays* 5:137-155 (1995).
- [10] Lin, K.-C., Kennedy, P.J., and Jackson, T.A., "Spray Structures of Aerated-Liquid Jets in Subsonic Crossflows," AIAA Paper 2001-0330, 39th AIAA Aerospace Sciences Meeting, Jan. 2001.
- [11] Gautam, V. and Gupta, A. K., "Transient cryogenic flow and mixing from a coaxial rocket injector," AIAA Paper 2007-573, 45th AIAA Aerospace Sciences Meeting and Exhibit, Reno, NV, 8-11 January 2007.
- [12] Santoro, R. J., "Applications of laser-based diagnostics to high pressure rocket and gas turbine combustor studies," AIAA Paper 98-2698, 20th AIAA Advanced Measurement and Ground Testing Technology Conference, Albuquerque, NM, 15-18 June 1998.
- [13] Klimenko, D. N., Clauss, W., Mayer, W., Oswald, M., and Smith, J. J., "Optical diagnostics and instrumentation for supercritical combustion studies in LOX/H₂ rocket engine combustion chamber," 20th International Congress on Instrumentation in Aerospace Simulation Facilities, 2003.
- [14] Rachner, M., Becker, J., Hassa, C., and Doerr, T., "Modeling of the Atomization of a Plain Liquid Fuel Jet in Crossflow at Gas Turbine Conditions," *Aerospace Science and Technology*, Vol. 6, 2002, pp. 495-506.
- [15] Strakey, P. A., Talley, D. G., and Hutt, J.J., "Mixing Characteristics of Coaxial Injectors at High Gas/Liquid Momentum Ratios," *Journal of Propulsion and Power*, Vol. 17, 2001, pp. 402-410.
- [16] Woodward, R. D., Pal, S., Farhangi, S., Jensen, G. E., and Santoro, R. J., "LOX/GH₂ Shear Coaxial Injector Atomization Studies: Effect of Recess and Non-Concentricity,"

AIAA Paper 2007-571, 45th AIAA Aerospace Sciences Meeting and Exhibit, Reno, NV, 8-11 January 2007.

- [17] Mayer, W. O. H., “Coxial atomization of a round liquid jet in a high speed gas stream: A phenomenological study,” *Experiments in Fluids*, Vol. 16, 1994, pp. 401-410.
- [18] Powell, C.F., Yue, Y., Poola, R., and Wang, J., “Time-Resolved Measurements of Supersonic Fuel Sprays Using Synchrotron X-rays,” *J. Synchrotron Radiation (Fast Communications)* 7:356-360 (2000).
- [19] MacPhee, A.G., Tate, M.W., Powell, C.F., Yue, Y., Renzi, M.J., Ercan, A., Narayanan, S., Fontes, E., Walther, J., Schaller, J., Gruner, S.M., and Wang, J., “X-ray Imaging of Shock Waves Generated by High-Pressure Fuel Sprays,” *Science* 295:1261-1263 (2002).
- [20] Cai, W., Powell, C.F., Yue, Y., Narayanan, S., Wang, J., Tate, M.W., Renzi, M.J., Ercan, A., Fontes, E., and Gruner, S.M., “Quantitative Analysis of Highly Transient Fuel Sprays by Time-Resolved X-radiography,” *Applied Physics Letters* 83(8): 1671-1673 (2003).
- [21] Qun, S., Lee, W-K., Fezzaa, K., Chu, Y.S., De Carlo, F., Jemian, P., Ilavsky, J., Erdman, M., and Long, G., “Dedicated Full-Field X-Ray Imaging Beamline at Advanced Photon Source,” *NIM A* 582 (1):77-79 (2007).
- [22] Wang, Y., Liu, X., IM, K., Lee, W., Wang, J., Fezzaa, K., Hung, D. L. S., Winkelman, J. R., “Ultrafast X-ray study of dense-liquid-jet flow dynamics using structure-tracking velocimetry,” *Nature Physics*, 27 January 2008.
- [23] Paciaroni, M, and Linne, M.A., “Single-Shot Two-Dimensional Ballistic Imaging through Scattering Media,” *Applied Optics* 43:5100-5109 (2004).

- [24] Sedarsky, D.L., Paciaroni, M.E., Linne, M.A., Gord, J.R., and Meyer, T.R., “Velocity Imaging for the Liquid-Gas Interface in the Near Field of an Atomizing Spray: Proof Of Concept,” *Optics Letters* 31:906-908 (2006).
- [25] Gord, J.R., Meyer, T.R., and Roy, S., “Applications of Ultrafast Lasers for Optical Measurements in Combusting Flows,” *Annual Review of Analytical Chemistry* (in press), July 2008.
- [26] Paciaroni, M., Hall, T., Delpanque, J-P., Parker, T., and Linne, M., “Single shot two-dimensional ballistic imaging of the liquid core in an atomizing spray,” *Atomization Sprays* **16**, 51-70 (2006).
- [27] Linne, M., Paciaroni, M., Hall, T., and Parker, T., “Ballistic imaging of the near field in a diesel spray,” *Exp. Fluids* **40**, 836-846 (2006).
- [28] Ho, P. P. and Alfano, R. R., “Optical Kerr effect in liquids,” *Phys. Rev. A* **20**, 2170-2187 (1979).
- [29] Sala, K. and Richardson, M. C., “Optical Kerr effect induced by ultrashort laser pulses,” *Phys. Rev. A* **12**, 1036-1047 (1974).
- [30] Wang, L. M., Ho, P.P., and Alfano, R. R., “Double-stage picosecond Kerr gate for ballistic time-gated optical imaging in turbid media,” *Applied Optics* **32**, 535-540 (1993).
- [31] Mujumdar, S. and Ramachandran, H., “Imaging through turbid media using polarization modulation: dependence on scattering anisotropy,” *Opt. Commun.* **241**, 1-9 (2004).
- [32] Liu, F., Yoo, K. M., and Alfano, R. R., “Ultrafast laser-pulse transmission and imaging through biological tissues,” *Applied Optics* **32**, 554-558 (1993).

- [33] Paciaroni, M., Hall, T., Delpanque, J.-P., Parker, T., and Linne, M., "Single-Shot Two-Dimensional Ballistic Imaging Of The Liquid Core In An Atomizing Spray," *Atomization Sprays*, Vol. 16, No. 1, 2006, pp. 51-70.
- [34] Kempe, M., Genack, A. Z., Rudolph, W., and Dorn, P., "Ballistic and diffuse light detection in confocal and heterodyne imaging systems," *J. Opt. Soc. Am. A* **14**, 216-223 (1997).
- [35] Cohn, R.K., Danczyk, S.A., and Bates, R.W., "A Comparison of the Performance of Hydrocarbon Fuels in a Uni-Element Combustor," AIAA Paper No. 2003-4752, *39th AIAA/ASME/SAE/ASEE Joint Propulsion Conference and Exhibit*, Huntsville, AL, July 20-24, 2003.
- [36] Cheng, G.C., Davis, R.R., Johnson, C.W., Muss, J.A., Greisen, D.A., and Cohn, R.K., "Development of GOX/Kerosene Swirl-Coaxial Injector Technology," AIAA Paper No. 2003-4751, *39th AIAA/ASME/SAE/ASEE Joint Propulsion Conference and Exhibit*, July 20-24, 2003.

ACKNOWLEDGEMENTS

Funding for this work was provided, in part, by the Air Force Research Laboratory under a subcontract from Innovative Scientific Solutions, Inc. This material is declared a work of the U.S. Government and is not subject to copyright protection in the United States.

I would like to take this opportunity to express my thanks to those who helped me with various aspects of conducting research and the writing of this thesis. First and foremost, Dr. Terrence R. Meyer for his guidance, patience and support throughout this research and the writing of this thesis. His insights and words of encouragement have often inspired me and renewed my hopes for completing my graduate education. I would also like to thank my committee members for their efforts and contributions to this work: Dr. Song-Charng Kong and Dr. Hui Hu.

Lastly and perhaps most importantly, many thanks go out to my family as they have always been there to encourage and help me pursue my education. My mother, father, sister, and brother have played an instrumental part in helping me become who I am today. I would like to especially acknowledge my mother, father, and grandfather, Donald Peterson, for instilling in me an interest in math and science which led to me pursuing an advanced degree in a scientific discipline.

